16th AIAA/CEAS Aeroacoustic Conference and Exhibit

Farfield filtering and source imaging for the study of jet noise

M. Koenig[*] [†], A. Cavalieri[*] [‡], P. Jordan[*], J. Delville[*],
Y. Gervais[*], D. Papamoschou[§], M. Samimy[¶] & S. Lele[||]

We present an analysis of the sound field radiated by a high Mach number subsonic jet. The spatial and temporal structures of the sound field are filtered and studied, respectively, by means of Proper Orthogonal Decomposition (POD) and wavelet transforms. The first POD mode is shown to give a near-perfect representation of the fluctuation energy radiation at low angles (in the range $30^\circ \leq \theta \leq 50^\circ$), larger numbers of modes being necessary to completely reproduce the radiation characteristics at higher angles. The wavelet analysis shows, in agreement with previous studies, that the temporal structure of the sound field is characterised by localised high-amplitude events. We implement two threshold intermittency metrics which we use to filter the pressure signals based on the scalogram topology. By varying these metrics we characterise the intermittency of the pressure signals as a function of emission angle. We again find that the sound field can be divided into two families: the fluctuations radiated at low angles ($30^\circ \leq \theta \leq 50^\circ$) are characterised by higher levels of global intermittency (an intermittency metric defined with respect to the overall fluctuation energy) than the fluctuations radiated in the angular range $\theta \geq 60^\circ$. However, when Farge's Local Intermittency Measure (defined with respect to the local fluctuation energy at each scale) is used to analyse the data, the fluctuations at all angles show identical behaviour. Results also show that the spectral shapes associated with the high-amplitude events, at all emission angles, are less broadband than those of the unfiltered field, suggesting that the most important source dynamics are not as broadband as the Fourier spectrum would have one believe.

Using both the POD and wavelet-filtered signals we decompose the acoustic field into two components: a component which we loosely attribute to coherent structures (CS) and a residuum (R). We compare the CS and R components with the LSS and FSS proposed by Tam *et al.*[1] We find that neither of these filtering criteria produce a natural division of the acoustic field into two components which match the LSS and FSS shapes. We also show, in the appendix, that the three-microphone approach proposed by Nance & Ahuja[2] to split the acoustic field into two such pieces is very sensitive to the three microphones which are chosen to perform the operation.

Finally, we implement a source imaging algorithm, using the CS part of the farfield signature, for both the POD and wavelet-based filtering, in order to establish if our so-called CS signal ensemble can be associated with wavepacket-like sources. Results show that the CS component of our filtering can be associated with a wavepacket-like source mechanism.

I. Introduction

A striking characteristic of the sound field radiated by a jet is the angular dependence of the power spectrum, and this has led to the idea that there may be two different 'source' mechanisms at work in

[*]Institut Pprime, Branche Fluide, UPR 3346, CNRS, Université de Poitiers, ENSMA, France.
[†]SNECMA, Département acoustique, 77550 Moissy-Cramayel, France
[‡]Instituto Tecnológico de Aeronáutica, São José dos Campos, Brazil
[§]Departement of Mechanical and Aerospace Engineering, University of California Irvine, Irvine, CA, USA
[¶]Gas Dynamics and Turbulence Laboratory, The Ohio State University, Columbus, OH, USA.
[||]Department of Mechanical Engineering, Stanford University, Stanford, CA, USA

Copyright © 2010 by P. Jordan. Published by the American Institute of Aeronautics and Astronautics, Inc., with permission.

the production of sound by high-speed subsonic flows (see Tam *et al.*[1]). However, as argued by Jordan & Gervais,[4] while Tam's similarity spectra clearly hint at an intriguing peculiarity regarding the behaviour of a jet flow in the production of sound, the precise details of what this peculiar behaviour entails remain unclear. The recent paper by Tam *et al.*[1] argues for the existence of two distinctly different, statistically independent, kinds of 'source' activity, while other recent work by Leib & Goldstein[5] demonstrates that the farfield structure may also be explained by appealing to a difference in the way a single 'source' structure 'couples' with the farfield.

As early as 1972 (Crow & Champagne,[6] Moore,[7] Michalke & Fuchs,[8] Mankbadi & Liu[9]) the idea that coherent structures in jets may radiate in a manner similar to that of a convected wave-packet has been considered. Since that time, a considerable number of studies have pursued this line of thought. Tam *et al.*[1] use this analogy to explain the downstream radiation pattern of a jet, arguing that the sideline radiation is a result of statistically independent 'fine-scale' turbulence. It is interesting to ask two questions with regard to such descriptions of sound-sources in jets. Firstly, does farfield data support the idea of two statistically independent source mechanisms? And, secondly, what are the salient features of such sources, if they exist? For example, in the case of the wave-packet source, the answer to the second question which is most often provided appeals to the effect of spatial amplitude modulation, which, on account of the antenna-effect (Crow[10]) leads to constructive interference, resulting in a 'beaming' of sound energy in the downstream direction; in the spectral domain this amounts to the appearance of fluctuation energy with sonic phase velocity in the radiation direction(s).

A further interesting characteristic of sound production by subsonic round jets, which has been recognised for some time (Juvé *et al.*,[11] Guj *et. al.*,[12] Hileman *et al.*[13]), and which is now receiving closer attention, in terms of both analysis (Cavalieri *et. al.*,[14] Grassucci *et. al.*[15]) and modelling (Sandham *et al.*,[16] Cavalieri *et. al.*[17]), is its temporal intermittency: the most energetic sound producing events occur in temporally localised bursts. This means that Fourier frequency analysis is poorly adapted for an optimal description of both 'source' and sound: the projection of the space-time structure of either onto infinitely extended Fourier modes will tend to 'smear' the local details of the sound-production events across a large band of frequencies; the most salient local details may thus be lost. Furthermore, this observation raises the question: is jet-noise really as broadband as the Fourier spectrum suggests - the spatiotemporal jittering of spatiotemporally localised, coherent events can produce a deceptively broad spectrum.

In this paper we address the above questions by effecting decompositions of the farfield radiated by subsonic jets. We endeavour to do so in as objective and unbiased a manner as possible, to see what the data has to say for itself. We choose Proper Orthogonal Decomposition to assess the spatial structure of the farfield, and wavelet transforms to assess the temporal structure. Each tool is used to ask a specific question. In the case of POD our reasoning is as follows: if statistically independent source mechanisms are simultaneously operative within a jet, it should be possible to discern this purely by statistical analysis of simultaneous multi-microphone data. The simplest and arguably least biased approach is to look at the POD modes (or principal components) of the data. How effective are the POD modes in compressing, i.e. explaining or fitting, the instantaneous pressure data? In the case of the wavelet decomposition, we seek to quantify the temporal intermittency of the farfield as a function of polar angle; and, in particular we study the spectral shape and directivity of the high-energy bursts which are known to populate the time-histories of pressure fluctuations recorded by farfield microphones.

By means of these analysis procedures it is possible to decompose the farfield into different components: the POD analysis allows a decomposition into a component associated with the first principal component of the farfield (the 1st POD mode) and a residuum (all of the other modes); the wavelet analysis allows the farfield to be decomposed into components associated with the high-energy bursts and a residuum. In this paper we will loosely refer to the two components of our decomposition as CS (for coherent structure) and R (for residuum). We study the directivity and spectral shapes of the two components, and we apply a source imaging algorithm, as used by Papamoschou,[3] in order to see if the CS component can be thought of as the signature of a wavepacket source.

Results obtained with both filtering operations suggest a separation of the acoustic field into two families, associated, respectively, with low- and high-angle radiation. However, neither of the filtering operations provide a clear split of the data into something matching the Large-scale and Fine-scale similarity spectra (LSS and FSS) shapes of Tam *et al.*[1] We also apply the three-microphone approach of Ahuja to the data, and find it to be quite sensitive to the three microphones which are chosen to perform the operation. Finally, application of the source imaging technique shows that the CS signature obtained with both the POD- and wavelet-based filtering operations can be thought of as associated with a wavepacket-like source.

II. Experiment

The experiments reported in this paper were performed at the MARTEL facility of the CEAT (Centre d'Etudes Aérodynamiques et Thermiques), Poitiers, France on a 0.05 m diameter cold jet at Mach 0.9 (Reynolds number of 10^6). The acoustic field was sampled using an arc of 12 microphones at a distance of 30 diameters from and centred on the jet exit. The angular position of the microphones varies from 30° to 140° with respect to the downstream jet axis. The acoustic setup is shown in figure 1. For further details see Jordan *et al.*[18]

Figure 1. Acoustic measurement setup.

The Power spectra for the 12 microphones are shown in figure 2. The characteristic LSS (Large-Scale Spectrum) and FSS (Fine-Scale Spectrum) shapes are observed, respectively, at low and high emission angles.

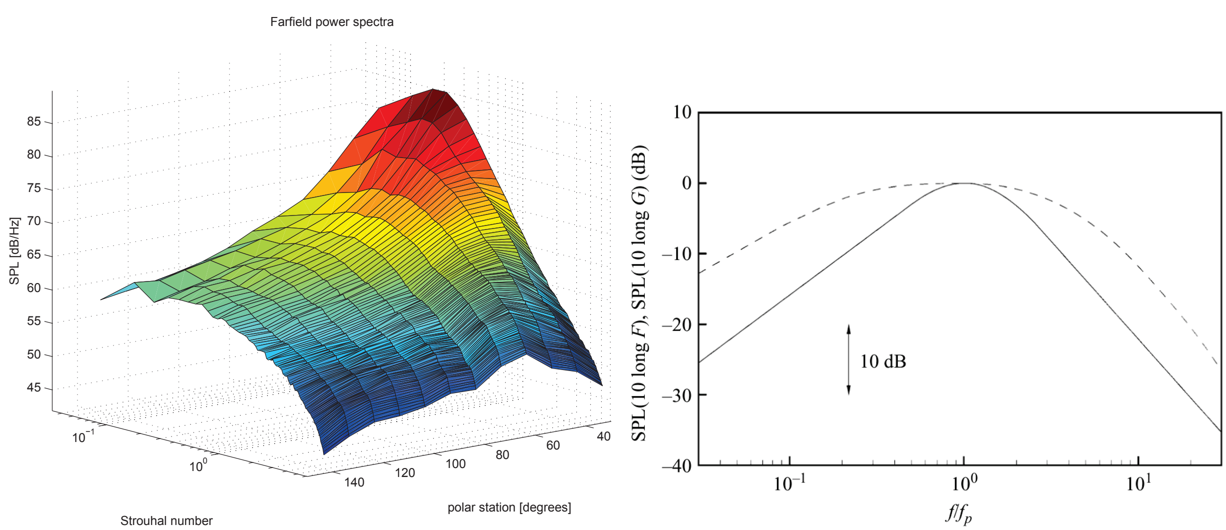

Figure 2. (a) Power Spectra, $Spp(\theta, f)$ of the Mach 0.9 cold jet ; (b) Similarity spectra for the two components of turbulent mixing noise.——, large turbulence structures/instability waves noise;— – —, fine-scale turbulence noise (Tam *et al.*[1]).

III. Analysis methodology

As outlined in the introduction, we aim to study and subsequently decompose the farfield of the jet by appealing to both its spatial (polar) and temporal structures. POD and wavelet transforms are used to achieve this.

A. POD analysis

In the case of farfield jet noise, temporal POD (whose Kernel is a spatial correlation at zero time-delay $p(\theta_i, \tau_i = 0)p(\theta_j, \tau_j = 0)$) is of limited use, because the microphone signals are more or less de-correlated at zero time delay. The cross-correlation matrix is therefore diagonal, the corresponding eigenfunctions resemble Dirac functions (each with a peak at a given microphone location), and the spectra of the expansion coefficients correspond, approximately, to the microphone spectra. We therefore use spectral POD to decompose the sound field. In this case the kernel of the POD problem is the cross-spectral matrix (hereafter CSM) $G(\theta_i, \theta_j, \omega)$:

$$G(\theta_i, \theta_j, \omega) = < p(\theta_i, \omega).p^*(\theta_j, \omega) >, \tag{1}$$

where <> denotes ensemble averaging. The Fredholm integral is solved one frequency at a time, providing us with frequency-dependent eigenvalues and eigenvectors. The spatial phase of the soundfield is thus captured at each frequency, and this information is contained in the shapes of the eigenfunctions (which are complex). The temporal phase is lost, but it can be recovered later by projecting the original data onto the eigenfunctions.

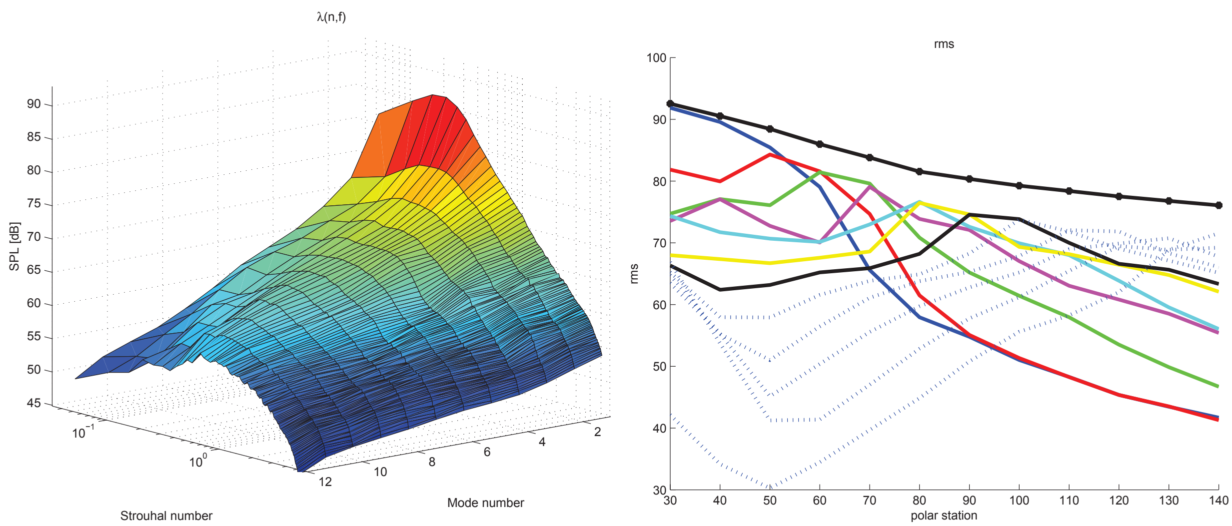

(a) (b)

Figure 3. (a) Eigenspectra, $\lambda_i(f)$; (b) rms (total and per n) ; black dots = baseline rms ; black line = sum of POD modes ; colored lines = contribution of each POD mode ; Blue : n=1 ; Red : n=2, . . .

The frequency dependent eigenvalues are shown in figure 3(a). We see that the first eigenmode captures a very large portion of the energy, particularly at the peak frequency, and has a 'peaky' spectral shape. The higher order modes are more broadband. The directivity of the modes is shown in figure 3(b). Mode 1 clearly dominates the downstream radiation, and has a shape characteristic of a wave-packet type source. The remaining modes have gradually changing spectral shapes and directivity patterns. This decomposition certainly appears to isolate an important dominant source mechanism with spectrum and directivity of the form of the first POD mode; however, there is no clear second mode which might correspond to something which could be clearly associated with a second, statistically independent 'source' mechanism.

Decomposition into CS and R components

Based on the directivity of the POD modes we will retain the first POD mode as our CS component, the remaining modes being lumped together and called R:

$$p_{CS}(\theta,t) = p(\theta,t)^{(1)} \quad \text{and} \quad p_R(\theta,t) = \sum_{k=2}^{N_{mod}} p(\theta,t)^{(k)}. \tag{2}$$

The directivities of the CS and R components are shown in figure 4.

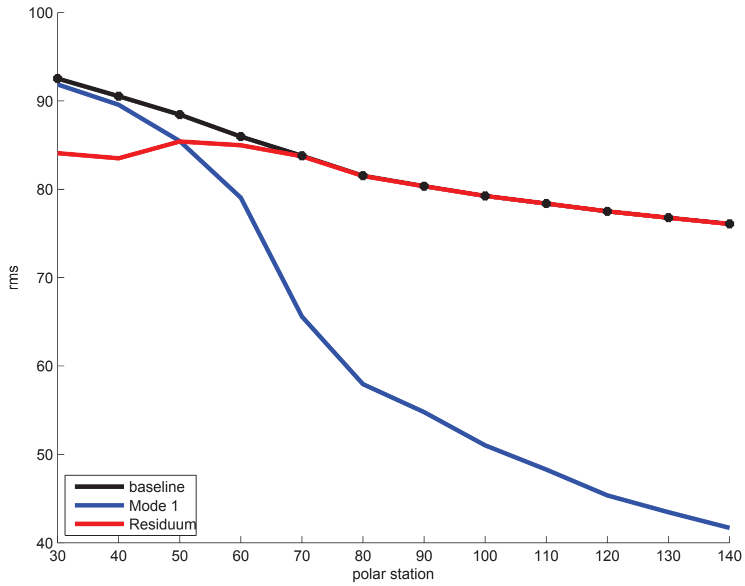

Figure 4. Rms ; black line = baseline ; blue line = CS ; red line = R (mode 2 to mode 12).

Figure 5 shows the spectral shape of the CS and R components as a function of polar angle; the LSS and FSS shapes are also shown. The spectral shape of the CS signature at 30 and 40 degrees shows a similar trend to the overall radiation, in so far as both peak at the peak frequency of the overall sound field, and the 30 degree signature is more narrowband than that observed at 40 degrees. At 50 degrees we see very similar spectral shapes and levels for both components, whereas for $\theta \geq 60°$ there is a clear dominance of the R component, whose shape fits the data. So, this filtering operation does not produce a match to the LSS and FSS.

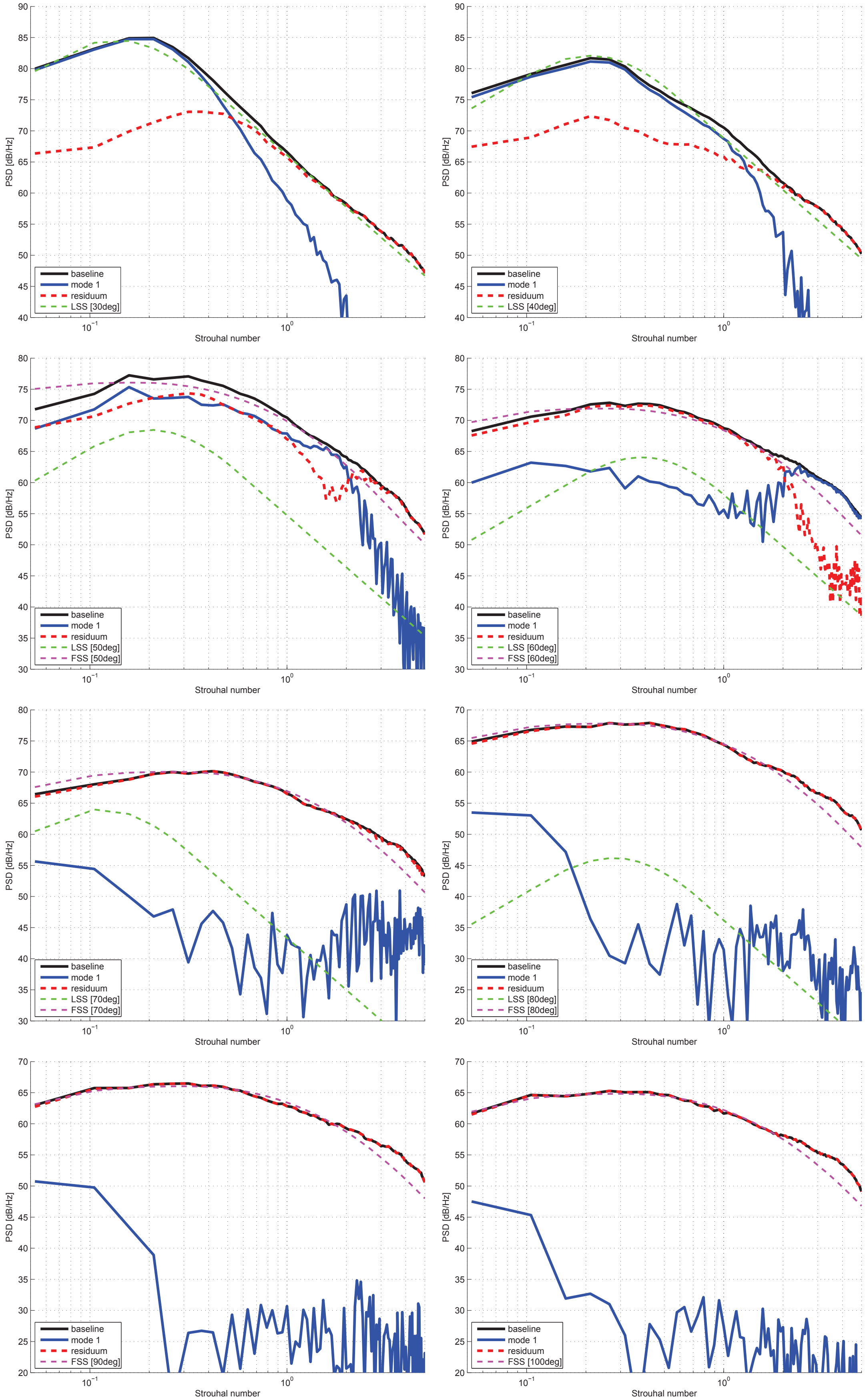

Figure 5. Autospectra of CS component (blue line) and R component (red) versus Tam's LSS (green) and FSS (magenta) from 30° to 100°.

Time-domain reconstruction of the CS and R components

To perform the imaging procedure developed in the next section, it is necessary to build the cross spectral matrix for each of the filtered components. As a consequence, the pressure signals associated with each POD mode must be reconstructed for each microphone. The contribution of a mode n in the frequency domain can be obtained by the following equation (for the inner product defined with the POD):

$$\hat{p}^{(n)}(\theta, f) = \hat{a}^{(n)}(f)\hat{\Phi}_p^{(n)}(\theta, f), \tag{3}$$

where the projection coefficients $\hat{a}^{(n)}(f)$ are:

$$\hat{a}^{(n)}(f) = \int_D \hat{p}(\theta, f)\hat{\Phi}_p^{*(n)}(\theta, f)d\theta, \tag{4}$$

D is the spatial domain of the POD and $\hat{\Phi}_p^{(n)}$ is the eigenvector of order n of p. The inverse Fourier transform of equation 3 gives us the temporal signal by mode for each spatial location $p(\theta, t)^{(n)}$. Figure 6 compares the original signal with the CS and R components for two different angles.

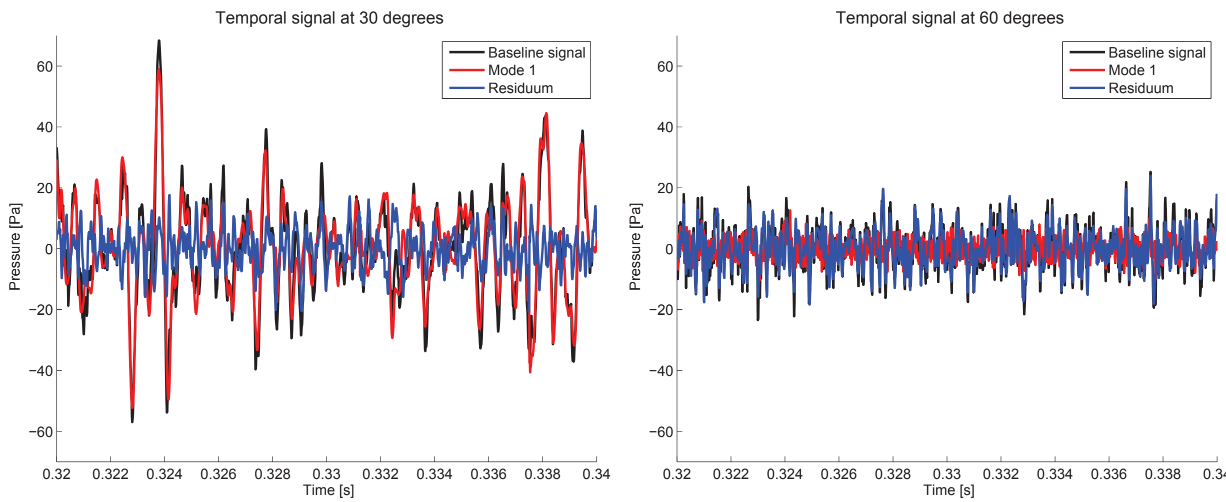

(a) (b)

Figure 6. Temporal reconstruction of the CS and R components of the pressure signals at (a) 30° (b) 60°.

B. Wavelet analysis

An analysis of the pressure signals by means of a continuous wavelet transform is performed so as to extract high-energy, intermittent events. The equations used to perform such a transformation are here briefly presented. For more information the reader can refer to Farge.[19] The continuous wavelet transform of the pressure signal is:

$$\tilde{p}(s, t) = \int_{-\infty}^{\infty} p(\tau)\psi(s, t - \tau)d\tau, \tag{5}$$

where s is the scale of the wavelet function. A Paul wavelet is used in this study, defined for s = 1 with an order m as (see Torrence *et al.*[20] for more details):

$$\psi(1, t - \tau) = \frac{2^m i^m m!}{\sqrt{\pi(2m)!}}[1 - i(t - \tau)]^{-(m+1)}. \tag{6}$$

The motivation for using a complex wavelet is that it better preserves the integrity of something which can be associated with a single "event", on account of that fact that the real and imaginary parts of the wavelet allow both high energy peaks and zero crossings associated with a given signature to contribute continually over an integral scale over which the event is active. Real wavelets will tend to break such single events into unphysical sub-events. The shape of Paul's wavelet for $m = 4$ in the temporal domain is shown in figure 7. Furthermore, this particular wavelet comprises shapes which are often observed in the sound pressure signatures of shear flows (see Juve *et al.*,[11] Guj *et al.*,[12] Hileman *et al.*,[13] Cavalieri *et al.*[14]) - it is thus useful for feature extraction.

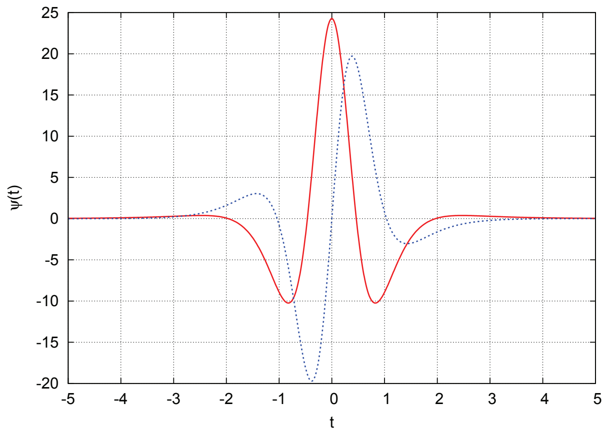

Figure 7. Paul's wavelet ; —— real part ; – – – imaginary part.

An example of scalograms of the pressure signals measured at 30° and 90° is shown in figure 8. For clarity, we only present a short time interval (0.1 s) of the signal (the original signal has a temporal length of ten seconds, and filtering is performed over the entire duration of the measurement). Before performing the wavelet transform, the signals are bandpass filtered to eliminate non-physical frequencies (lower than the cutoff frequency of the windtunnel for instance) and they are then normalised by the rms pressure at each angle so as to have a unit energy regardless of the observation angle. Also note that the scale s is converted to a pseudo-frequency f as in Torrence *et al.*[20] (which we then convert to a pseudo-Strouhal number):

$$f = (2m+1)/4\pi s$$
$$St = fD/U_j$$

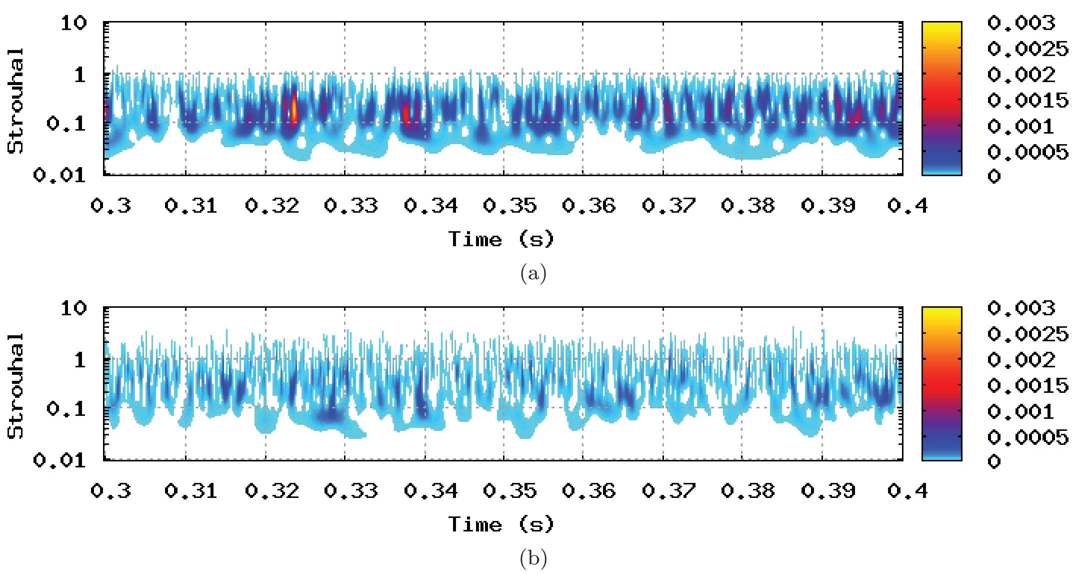

Figure 8. Wavelet scalogram $|\tilde{p}(s,t)|^2$ at (a) 30°;(b) 90°.

The 30° scalogram shows bursts of high-energy, temporally-localised activity, identified by the yellow/red spots. This is an indication of intermittent source activity where the downstream radiation is concerned.

The 90° scalogram on the other hand does not have such marked intermittent activity (the colour scales are directly comparable on account of the normalisation which has been effected). As discussed earlier, there is a difference between downstream and sideline radiation, which is well captured by the similarity spectra LSS and FSS. We here see that, in addition to the different spectral shapes, there is also a marked difference in intermittency between radiation to high and low emission angles; Fourier analysis necessarily misses this. If it amounts to an essential aspect of source mechanisms in jets, it needs to be explicitly modelled. Some work in this direction is reported by Sandham *et al.*[16] and Cavalieri *et al.*[17]

We now quantify this intermittency as a function of polar angle. We do so by introducing a threshold parameter which we use to decompose the pressure signals into CS and R components [a]. Filtering is performed using two criteria, each of which provides a different information regarding the temporal structure of the pressure signature considered: (1) Global Intermittency Measure ; and, (2) Local Intermittency Measure

Global Intermittency Measure

The Global Intermittency Measure (GIM) allows us to identify temporally- or scale-localised events which make large contributions to the overall fluctuation energy. The following filtering operation is effected:

$$\tilde{p_f}(\theta, s, t) = \begin{cases} \tilde{p}(\theta, s, t) & \text{if } |\tilde{p}(\theta, s, t)|^2 > \alpha \\ 0 & \text{if } |\tilde{p}(\theta, s, t)|^2 < \alpha \end{cases} . \tag{7}$$

The threshold α has units of energy density in the wavelet domain. As the total energy of each signal is normalised, the integration of the energy density in time and in scale is equal to unity. However, the distributions of the energy density in the scalogram may be completely different. Thus, for a given value of the threshold, more energy will be retained by the filtering for a peaky scalogram than for a flat one, and the relationship between the total filtered energy and the threshold is a quantitative measure of how 'peaky' the scalogram is. Peaks in the scalogram may arise on account of two kinds of signal characteristic: if a signal has intermittent bursts, there will be an energy concentration in the time direction of the scalogram; if, on the other hand, a signal has a pure frequency, such as a sine wave, there will be a concentration in the scale direction. If both conditions are verified, we have high concentrations in a limited region in both s and t. In this case, this is due to a high correlation of the original signal with a particular scale during a limited time interval. Physically, this corresponds to the presence in the temporal time series of a high-amplitude acoustic wave-packet, whose shape is well described by the wavelet function. The GIM metric will tend to highlight such events.

Local Intermittency Measure

The LIM[19] is defined as follows:

$$I(\theta, s, t) = \frac{|\tilde{p}(\theta, s, t)|^2}{< |\tilde{p}(\theta, s, t)|^2 >_t}, \tag{8}$$

where the $<>_t$ operator indicates an average of the scalogram in the t direction. As this average is performed independently for each scale, the local intermittency measure indicates, for a given scale, and regardless of its absolute energy density, if there are energy concentrations in the temporal direction; an energy concentration purely in scale, such as in a sine function, leads to an intermittency measure equal to one for all s and all t, which indicates that there are no intermittent bursts.

The filtering based on the local intermittency measure is again defined based on a threshold β:

$$\tilde{p_i}(\theta, s, t) = \begin{cases} \tilde{p}(\theta, s, t) & \text{if } I(\theta, s, t) > \beta \\ 0 & \text{if } I(\theta, s, t) < \beta \end{cases} . \tag{9}$$

The relationship between the value of the β threshold and the total filtered energy is, as in the case of the filtering based on the energy density of eq. (7), a quantitative measure of the peaks in the distribution of the local intermittency factor. This corresponds now to the presence in the temporal time series of acoustic wave-packets of high amplitude *in relation to the average energy for each scale*; however, this amplitude may

[a]this procedure is similar to that used by Hileman *et al.*[13] to sort flow information into loud and quiet ensembles

be low in relation to the global energy.

Results of wavelet filtering

An example of a result of the GIM filtering operation is shown in figure 9 for a microphone at 30°. The value of α in this figure is such that the filtered signal retains 30% of the total fluctuation energy at 30°. Figure 10(a) shows the filtered scalogram at 30°. Figure 10(b) shows the 90° scalogram for a value of α which leads to retention of the same energy.

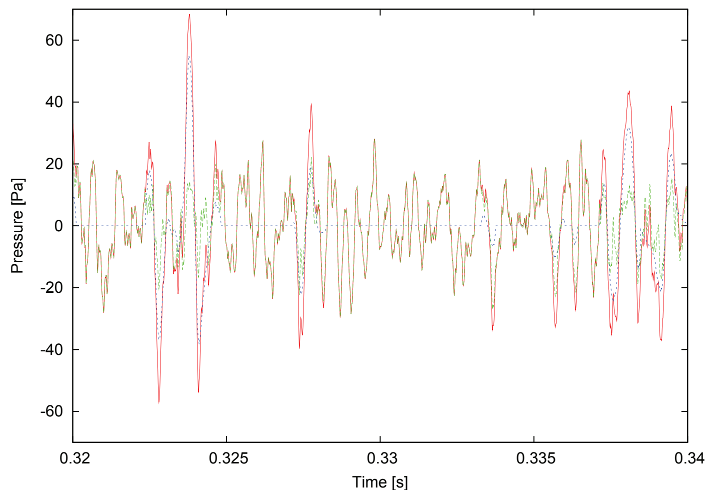

Figure 9. Temporal pressure signals at 30°: —— baseline ; – – – "filtered" ; – – – "residuum".

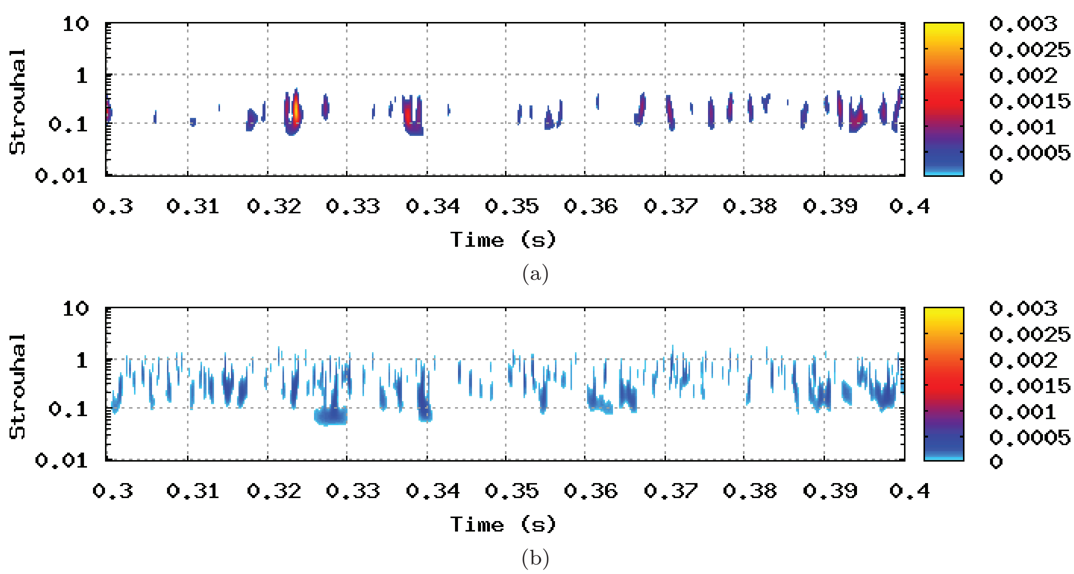

Figure 10. Filtered wavelet $|\tilde{p}(s,t)|^2$ scalogram at (a) 30°; (b) 90°.

The difference between the two filtered scalograms shows how the 30° signal receives contributions to its total fluctuation energy over shorter periods of high-amplitude activity; the 90° signal showing a more homogeneous temporal distribution.

Intermittency and fluctuation energy

Total energy is conserved under the wavelet transform and there exists the following equivalent of Parseval's theorem[20] for a given pressure signal localised at the angle θ :

$$\int_{\mathbb{R}} |p(t)|^2 dt = C_\psi^{-1} \int_{\mathbb{R}+} \int_{\mathbb{R}} |\tilde{p}(s,t)|.|\tilde{p}^*(s,t)| \frac{dsdt}{s^2} \tag{10}$$

where $p(t)$ is the time pressure signal for a given polar position θ, $\tilde{p}(s,t)$ its continuous wavelet transform and C_ψ is a constant associated with the wavelet function which we use. As the pressure signals are normalised by the *rms* value, the integrated energy of the scalograms, regardless of the angle considered, is equal to one. Calculation of the energy after either GIM or LIM filtering, using equation 10, gives us the ratio of energy which is conserved. Figure 11 shows the relationship between filtered energy and α and β for each of the microphones.

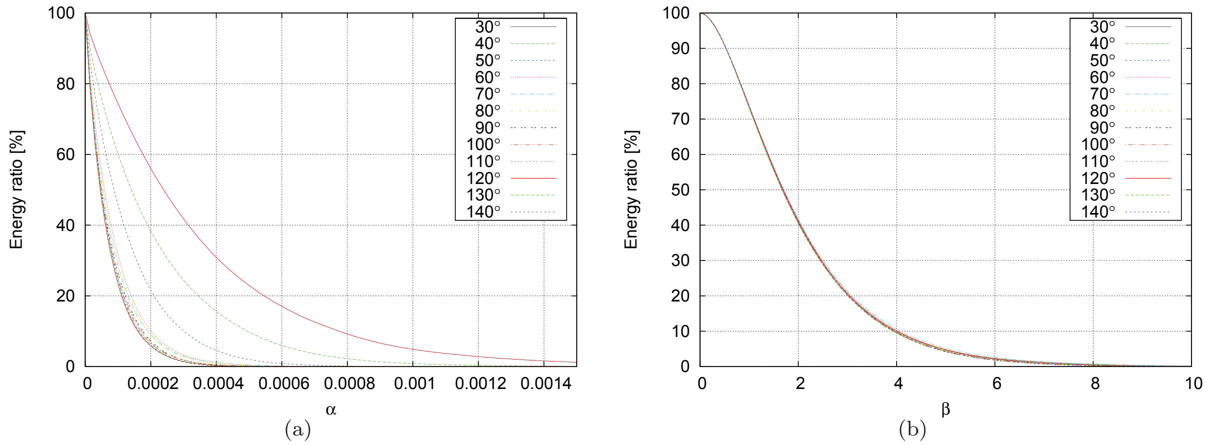

Figure 11. Energy ratio (filtered/residuum) as function of polar angle; (a) after GIM filtering; (b) after LIM filtering.

The GIM shows how the signals recorded in the angular range $60° \leq \theta \leq 140°$ comprise one family of curves. It is possible to conclude that these signals are characterised by similarly low levels of globally (energetically) important intermittency. In the angular range $30° \leq \theta \leq 50°$, on the other hand, we see a gradual evolution from high levels of GIM at 30° to lower levels similar to those of the low-energy family.

If we now consider the LIM-filtered data we see a very different picture: all of the curves collapse into a single family. This demonstrates that when we disregard contributions to the overall fluctuation energy, all of the scales of the farfield pressure signals are characterised by the same degree of temporal intermittency. This suggests that it is the acoustic efficiency of sources which is highly directional, rather than their absolute temporal structure.

Intermittency and active-time

We now study the impact of the filtering criteria on what we refer to as active time; by active time we mean the percentage of the time-history for which non-zero fluctuations are observed after the filtering operation has been applied. Figures 12 (a) and (b) show the result for the GIM and LIM filtering, respectively. The similarity with the previous result is striking: all microphones show a correlation between active-time and intermittent contribution to overall energy.

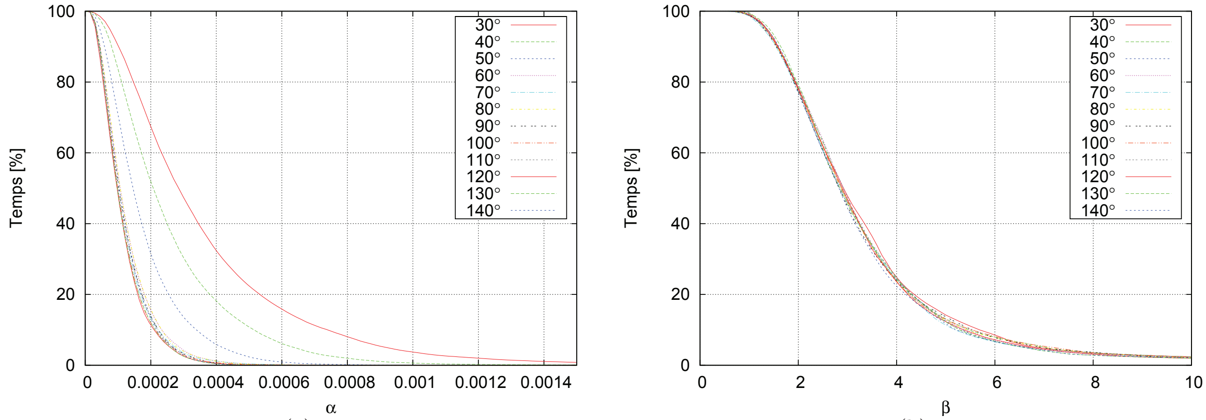

(a) (b)

Figure 12. Active time after : (a) GIM filtering; (b) LIM filtering.

Intermittency and spectral shape

After the filtering operation, it is possible to compute directivity and autospectra of the CS and R components. We choose two values of α. The first value is 0.00003, it corresponds to the value that best maintains the peak level of the CS component (and produces a similar result to that obtained by POD-filtering for the downstream microphones; but is dissimilar in so far as it produces a relatively omnidirectional radiation pattern (cf. figure 13)). The second value is 0.00015. This value is chosen because it provides a strong suppression of the fluctuations on the low-intermittency, 'sideline' family of microphones ($\theta \geq 60°$), whilst preserving between 30 and 70% of the fluctuation energy on the downstream family. The resulting spectra re shown in figures 14 and 15. Also, this level of α produces a CS directivity which is more directive in the downstream direction (cf. figure 13).

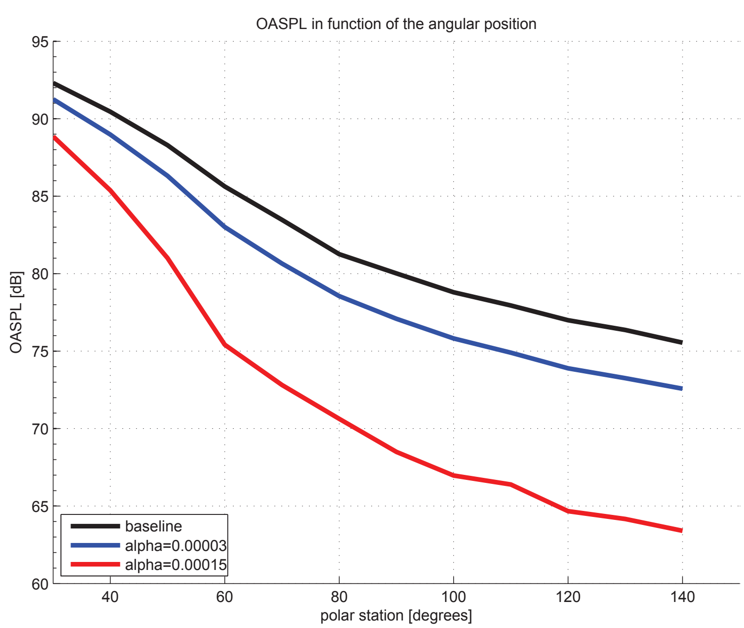

Figure 13. OASPL in function of the angular position. Black line = baseline; blue line = CS with $\alpha = 0.00003$; red line = CS with $\alpha = 0.00015$.

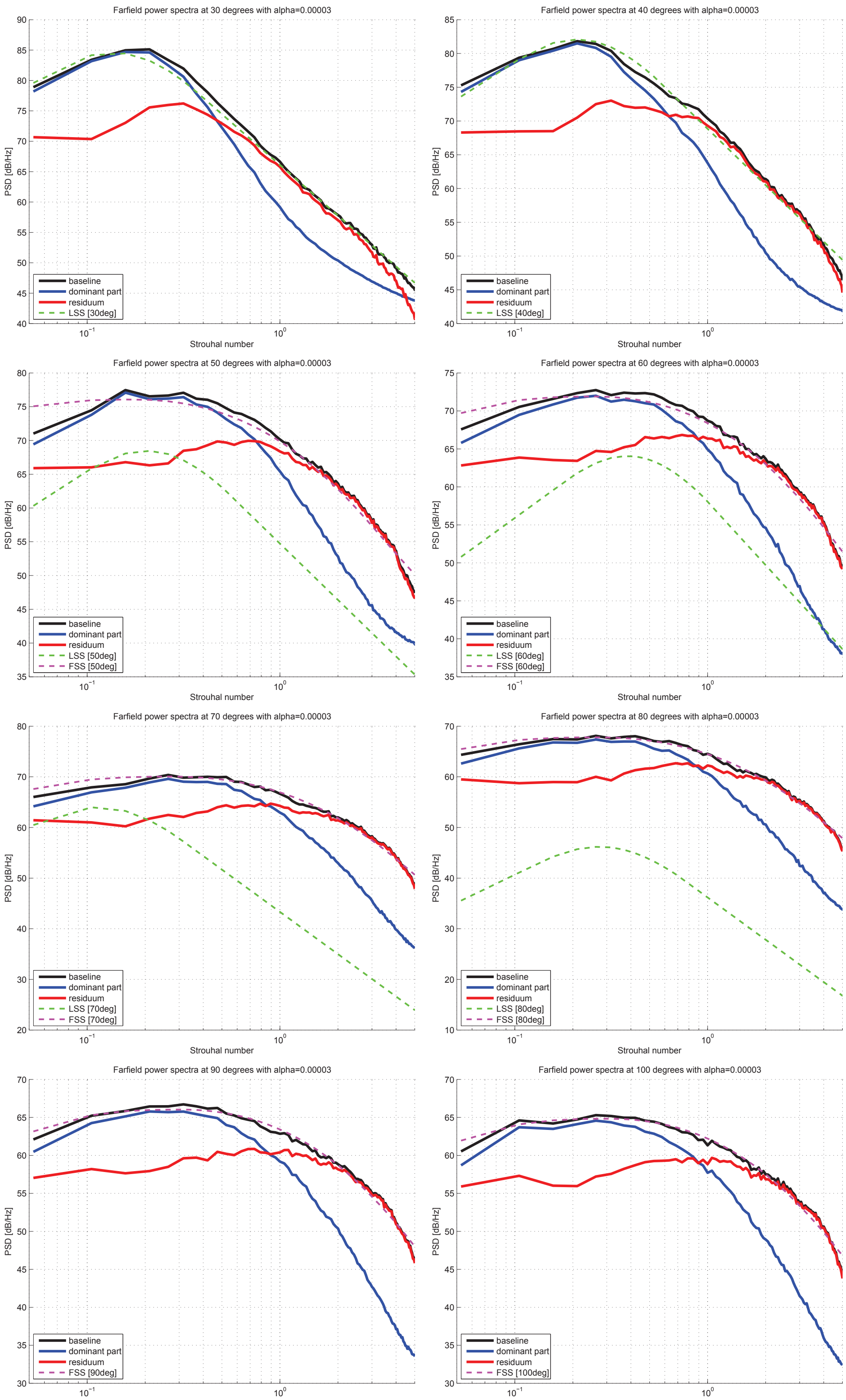

Figure 14. Autospectra of the CS component (blue) and R component (red) for $\alpha = 0.00003$ versus Tam's LSS (green) and FSS (magenta) from 30° to 100°.

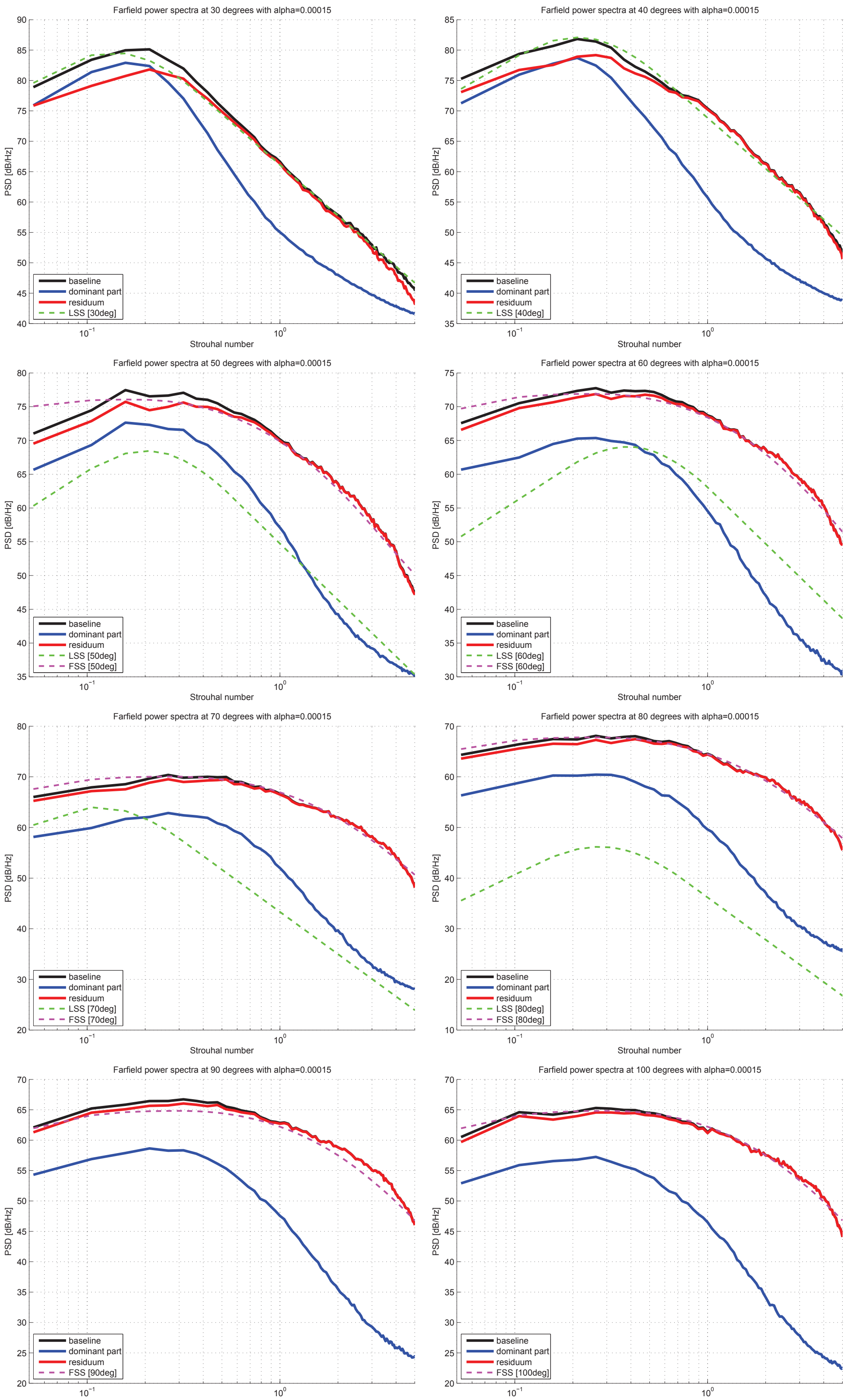

Figure 15. Autospectra of the CS component (blue) and R component (red) for $\alpha = 0.00015$ versus Tam's LSS (green) and FSS (magenta) from 30° to 100°.

In figures 14 and 15 we see that with the low level filtering ($\alpha = 0.00003$) the peak region of the CS spectrum agrees well with the baseline, higher frequencies being suppressed at all angles. As said, at low emission angles the CS-R decomposition resembles that of the POD. For the higher-level filtering ($\alpha = 0.00015$), the CS component is suppressed at higher emission angles, where the R-component dominates. At the higher angles there is some qualitative agreement in shape between the CS component and the LSS; however, at low emission angles there is no clear match.

IV. Imaging techniques

Source imaging techniques can be useful in providing insight regarding source mechanisms (cf. Papamoschou[3] for example), provided: (1) the ansatz used bears some similarity to the source mechanism; (2) the algorithm converges on a parameter set which is physically realistic. We use the imaging techniques here to assess if the CS components obtained by our filtering operations can be thought of as synonymous with the signature of a wavepacket-like mechanism.

A. Imaging procedure

For each of the models the procedure goes as follows. The cross-spectrum $< Q(\vec{y},\omega)Q^*(\vec{y}\,',\omega)) >$ of the sound source field is described in terms of a parameter vector A_k which is determined by "matching" the modelled and measured acoustics. Typically, the matching involves the cross-spectral matrix $G(\vec{x}_m,\vec{x}_n,\omega)$ where $\vec{x}_m$ and $\vec{x}_n$ denote the spatial locations of measurement points m and n, respectively. The experimental measurement of the CSM is denoted G_{exp}. The modeled CSM is $G_{mod}(A_k,\vec{x}_m,\vec{x}_n,\omega)$: it depends on the parameter vector A_k that describes the source model. Ideally, we would obtain A_k by setting :

$$G_{exp}(\vec{x}_m,\vec{x}_n,\omega) = G_{mod}(A_k,\vec{x}_m,\vec{x}_n,\omega) \tag{11}$$

and hope for an exact solution for A_k. This is rarely the case, so we instead resort to methods that minimise the difference between the modelled and measured acoustic fields. Concentrating on a given frequency ω, we define the error :

$$F(A_k) = \sum_{m,n=1}^{M} |G_{exp}(\vec{x}_m,\vec{x}_n) - G_{mod}(A_k,\vec{x}_m,\vec{x}_n)|^2 \tag{12}$$

where M is the total number of measuring stations. We seek a vector A_k that minimises $F(A_k)$. A method that has proven effective is the conjugate gradient minimisation method, particularly as implemented by Shanno and Phua.[21]

B. Simple wavepacket example

The wave source model is, in this case, simply a wavepacket like those in Crighton and Huerre.[22] On cylindrical surface $r = r_0$, the pressure is prescribed as follows :

$$p(r_0,x,t) = p_0(x,A_k)e^{-i\omega t}, \tag{13}$$

where $p_0(x,A_k)$ is an oscillatory function that amplifies and decays with x. We select an "asymmetric Gaussian" formulation for $p_0(x,A_k)$:

$$p_0(x,A_k) = \epsilon B(x)e^{i\alpha k}, \tag{14}$$

with

$$B(x) = \begin{cases} \exp(-b_1(x-x_0)^2), & x \le x_0 \\ \exp(-b_2(x-x_0)^2), & x > x_0 \end{cases} \tag{15}$$

The vector A_k is composed of five parameters (ϵ, α, b_1, b_2, x_0), characteristic of an asymmetric Gaussian curve, as we can see in the figure 16.

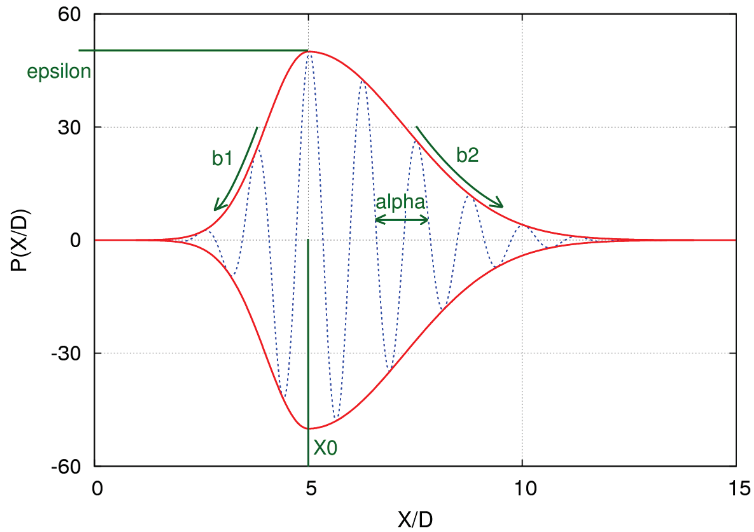

Figure 16. Asymmetric Gaussian curve using for the wavepacket model.

C. Results

POD filter

The results of the imaging technique for different Strouhal numbers (0.20 and 0.40) are shown in figure 17 and figure 18 respectively. We see how the result obtained using the CS signature agrees quite well with the result using the unfiltered data. This suggests that the filter was pertinent; and that it makes sense to think of the CS signature so obtained as something which corresponds to a wavepacket-like source.

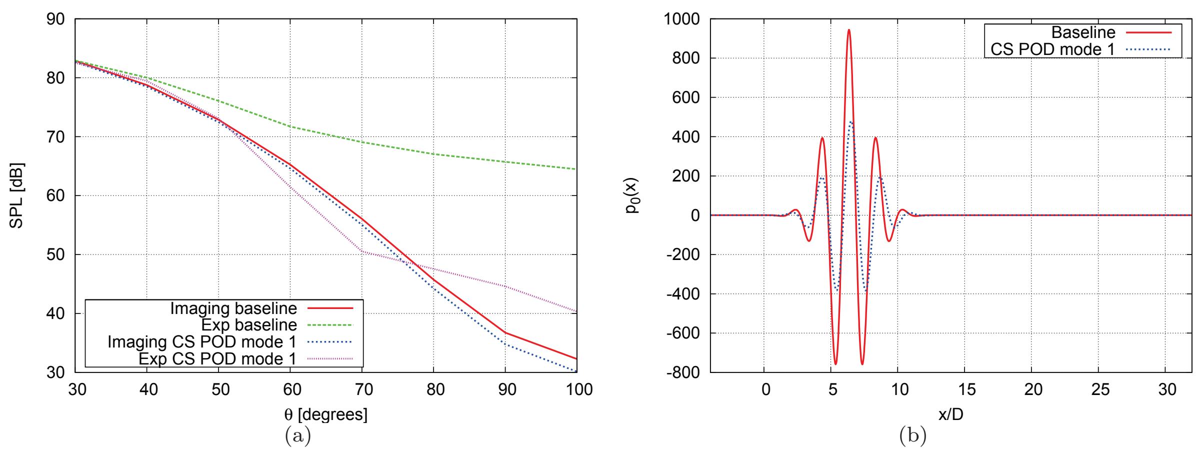

Figure 17. Results at Strouhal 0.20 : (a) Directivity ; (b) Resulting wavepacket(A_k).

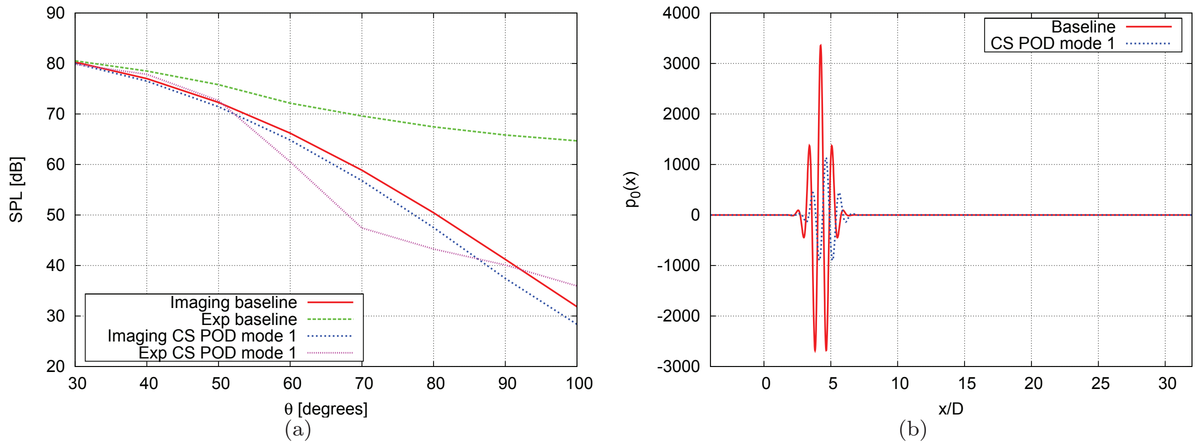

Figure 18. Results at Strouhal 0.40 : (a) Directivity ; (b) Resulting wavepacket(A_k).

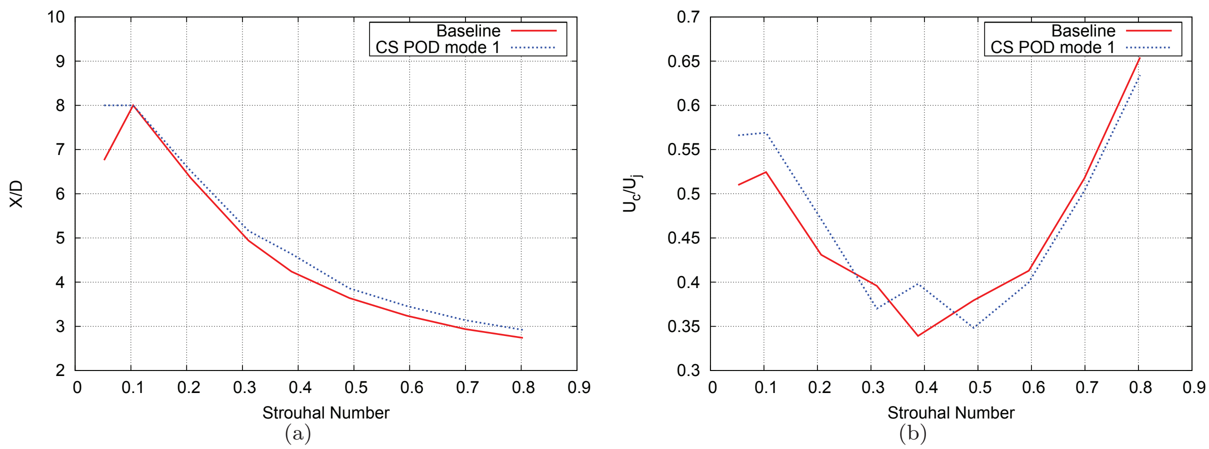

Figure 19. (a) Wavepacket center as a function of Strouhal number ; (b) convection velocity (scaled by the jet velocity) as a function of Strouhal number.

Wavelet GIM filter

The results of the imaging technique for different Strouhal numbers (0.20 and 0.4) are shown in figure 20 and figure 21 respectively. The result in this case, while not quite as good as that obtained with the POD, produces physically sensible results: the source positions and convection velocities are very close to those obtained with the unfiltered data, again suggesting that the filtering operation has some pertinence. The slightly poorer agreement obtained using the wavelet-based filter may be due to the fact that the CS signature so-obtained is intermittent, while the source *ansatz* used for the imaging can have no such intermittency. Future work will involve the use of more sophisticated source *ansatz*, such as described in Cavalieri et al.[17] for example.

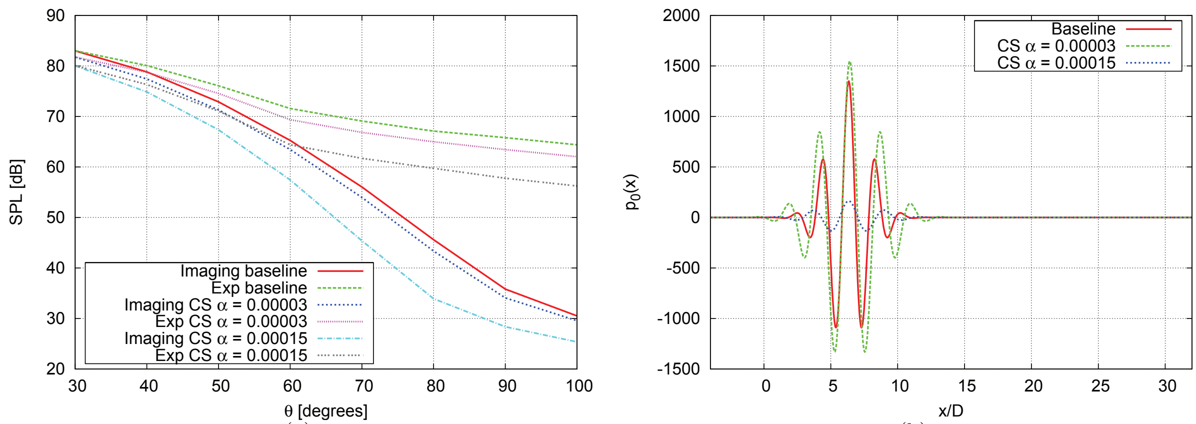

(a) (b)

Figure 20. Results at Strouhal 0.20 : (a) Directivity ; (b) Resulting wavepacket(A_k).

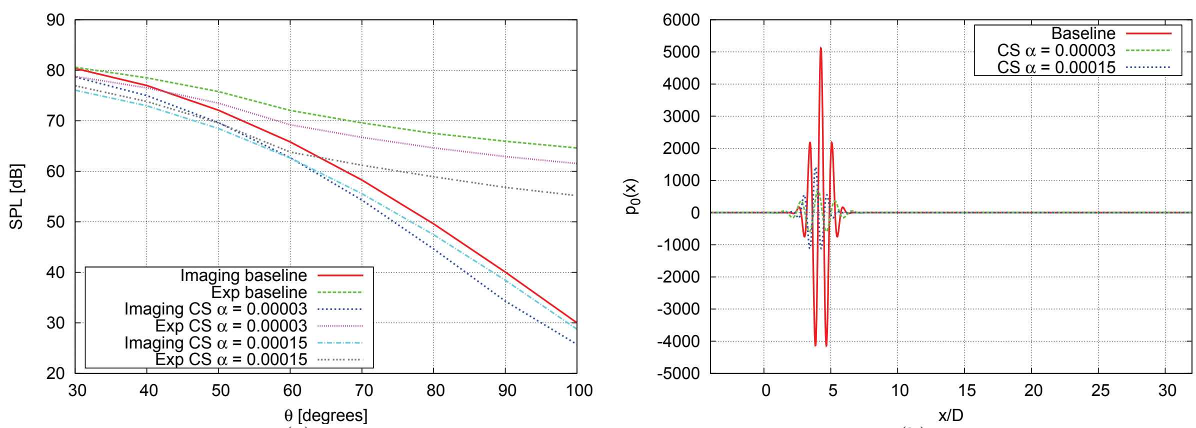

(a) (b)

Figure 21. Results at Strouhal 0.40 : (a) Directivity ; (b) Resulting wavepacket(A_k).

V. Conclusion and future work

An analysis of jet noise data has been presented where we perform different filtering operations aimed at gaining insight into the angular dependence of the spectral shape of the radiated sound field. POD is used to assess the spatial structure, wavelet transforms being used to study the temporal intermittency. Using each of these approaches, the sound field is decomposed into a component which we loosely associate with coherent structures (CS), and a residuum (R). Both of these filtering operations suggest differences between the downstream and sideline radiation; however, neither of them clearly split the field into two distinct components with characteristics similar to those of the LSS and FSS of Tam *et al.*[1] We furthermore find

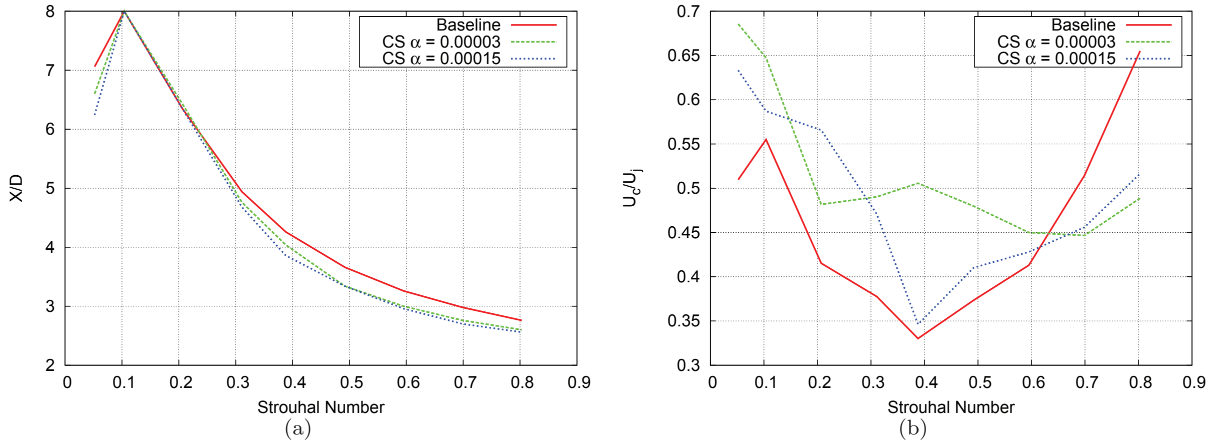

Figure 22. (a) Wavepacket center as a function of Strouhal number ; (b) convection velocity (scaled by the jet velocity) as a function of Strouhal number.

(appendix B) that results obtained using the three-microphone method applied by Nance & Ahuja[2] is rather sensitive to the three microphones which are chosen to perform the operation.

We implement a source imaging algorithm using both the unfiltered and CS-filtered signals. Results show that the CS-filtered data can be thought of as being associated with a wavepacket-like source. While not shown in this paper, imaging implemented using the R-filtered data does not lead to physically sensible results, suggesting that the R-filtered data does not correspond to wavepacket-like radiation.

Appendix A : impact of the mother wavelet.

We here show that the results obtained using the GIM intermittency metric are insensitive to the choice of mother wavelet.

$$\psi(t) = \frac{(-1)^{m+1}}{\sqrt{\Gamma(m+\frac{1}{2})}} \frac{d^m}{d\eta^m}\left(e^{-\eta^2/2}\right) \qquad \psi(t) = \pi^{-1/4} e^{i\omega_0 \eta} e^{-\eta^2/2} \qquad \psi(t) = \frac{2^m i^m m!}{\sqrt{\pi(2m)!}}(1-i\eta)^{-(m+1)}$$

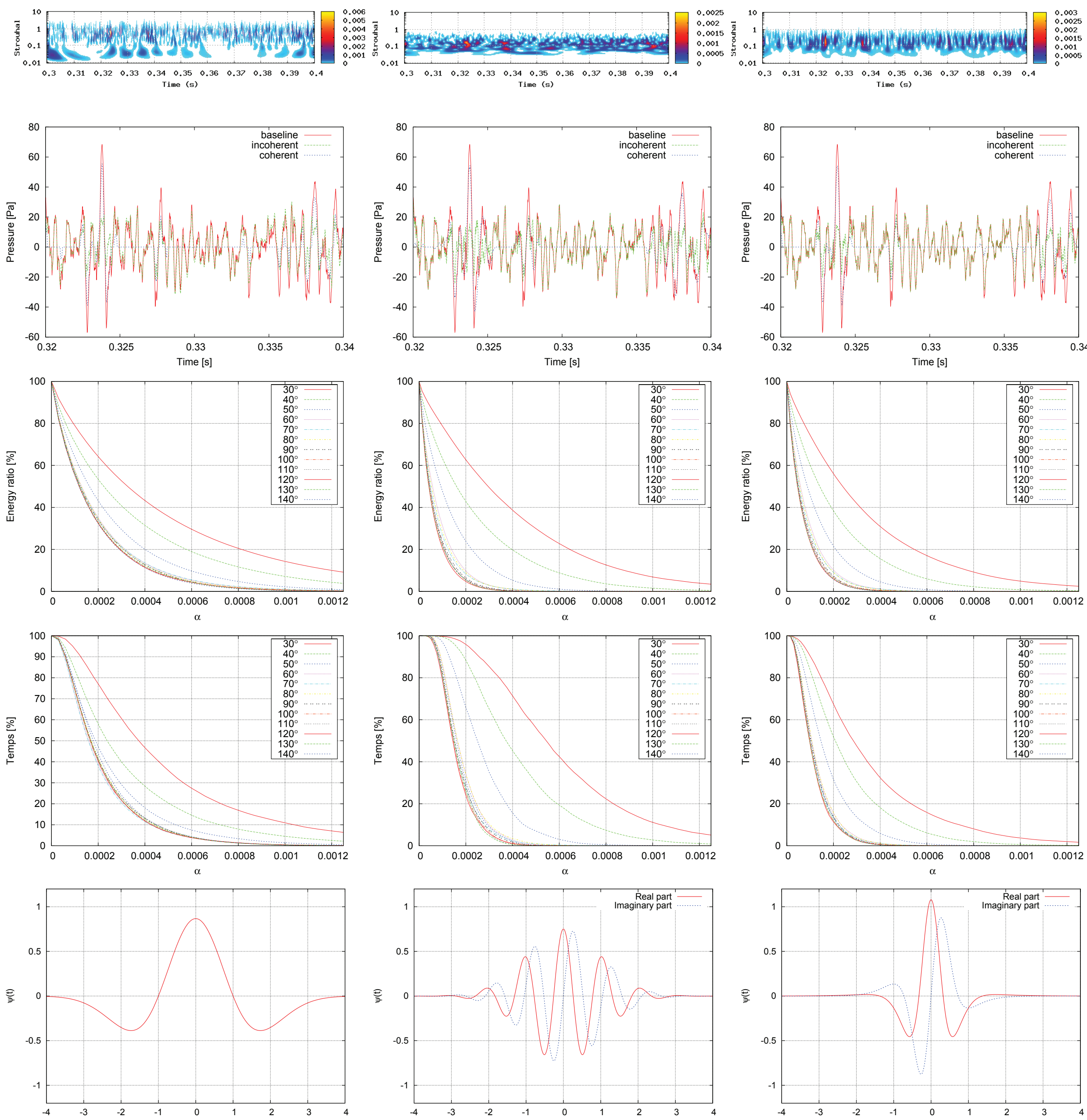

(a) (b) (c)

Figure 23. Wavelet comparisons : (a) Mexican hat (real) ; (b) Morlet (complex) ; (c) Paul (complex)

Appendix B : a coherence function method.

Coherence-based methods have been developed for identification and extraction of acoustic signals buried in other noise signals. In most aeroacoustic applications, the presence of uncorrelated extraneous noise is unavoidable. To overcome this, Chung[23] developed a three-microphone signal enhancement technique for rejecting transducer flow-noise interference. Figure 24 is a scheme of this method.

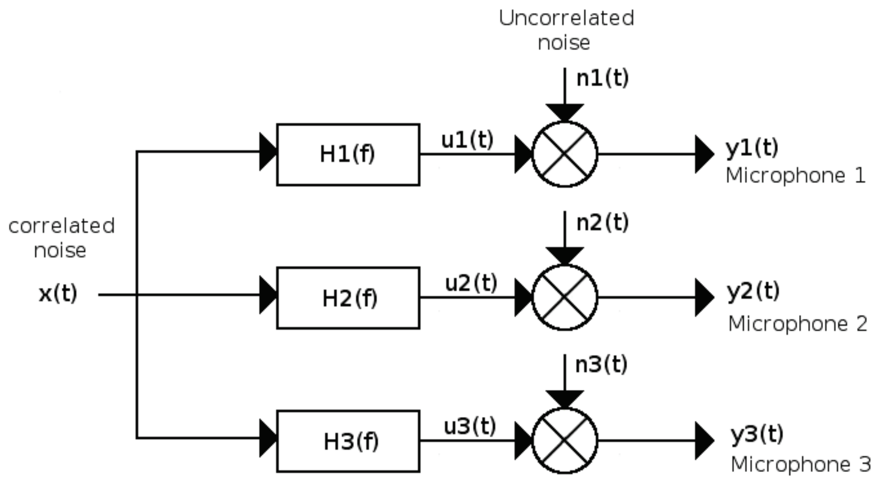

Figure 24. Schematic representation of the three microphones technique.

For more details about this method, the reader can refer to Nance & Ahuja[2] who applied this method on a Mach 0.9 round jet. The three-microphones technique decomposes the signals in correlated and uncorrelated noise. The spectral density functions of the correlated signals for the three microphones (denoted 1, 2 and 3) are then:

$$\begin{aligned} G_{u_1u_1} &= G_{y_1y_1}\frac{\gamma_{12}\gamma_{13}}{\gamma_{23}} \\ G_{u_2u_2} &= G_{y_2y_2}\frac{\gamma_{12}\gamma_{23}}{\gamma_{13}} \\ G_{u_3u_3} &= G_{y_3y_3}\frac{\gamma_{13}\gamma_{23}}{\gamma_{12}}, \end{aligned} \tag{16}$$

where γ_{ij} is the coherence function defined by:

$$\gamma_{ij}^2(\omega) = \frac{|Spp(\theta_i,\theta_j,\omega)|^2}{Spp(\theta_i,\theta_i,\omega)Spp(\theta_j,\theta_j,\omega)}. \tag{17}$$

And the spectral density of the uncorrelated signal for each microphone is:

$$\begin{aligned} G_{n_1n_1} &= G_{y_1y_1} - G_{u_1u_1} \\ G_{n_2n_2} &= G_{y_2y_2} - G_{u_2u_2} \\ G_{n_3n_3} &= G_{y_3y_3} - G_{u_3u_3} \end{aligned} \tag{18}$$

The coherence function for the 50° microphone is represented in figure 25. With no surprise, the highest correlations appear for the duo of microphones 50-60°and 40-50°that is to say the closest microphones. This observation will be fundamental afterwards.

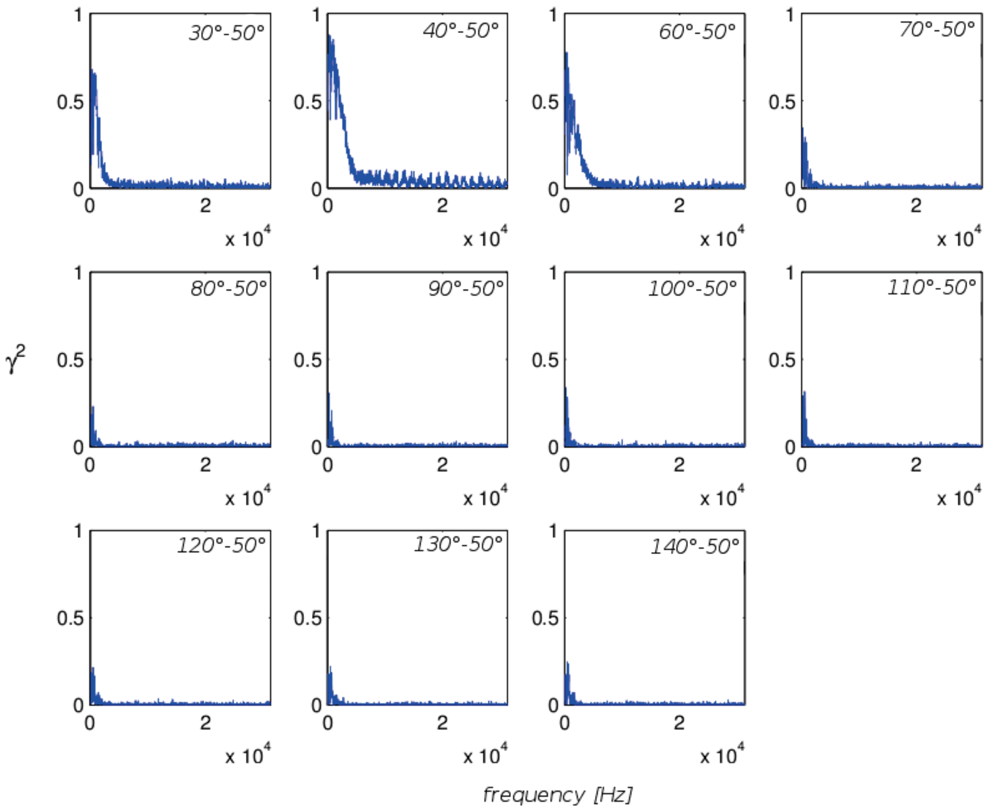

Figure 25. Coherence function for the 50° microphone.

We applied the three microphone technique of Nance & Ahuja at different angles for our database. The following figures 26, 27 and 28 present the results of this technique. In these figures, the F and G spectra correspond to the LSS and FSS spectra respectively. At low angles, 30° and 40° in figure 26, we choose to represent the autospectrum, the 'correlated' noise calculated with equation 16 and the Large-Scale Similarity Spectrum of Tam. There is a good match between Tam's LSS and the correlated noise.

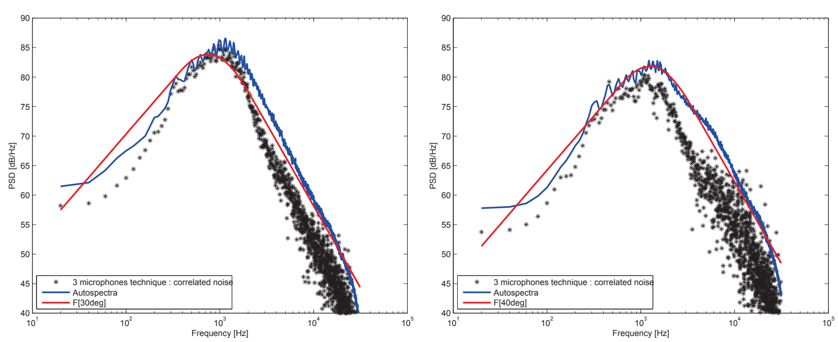

(a) (b)

Figure 26. (a) At 30° ; (b) At 40°.

At middle angles, 60° and 70° in figure 27, we represent the autospectra, the correlated and uncorrelated noises calculated with equation 16 and equation 18 respectively and Tam's LSS and FSS. There is a satisfactory match between Tam's LSS and the correlated noise and also between Tam's FSS and the uncorrelated noise.

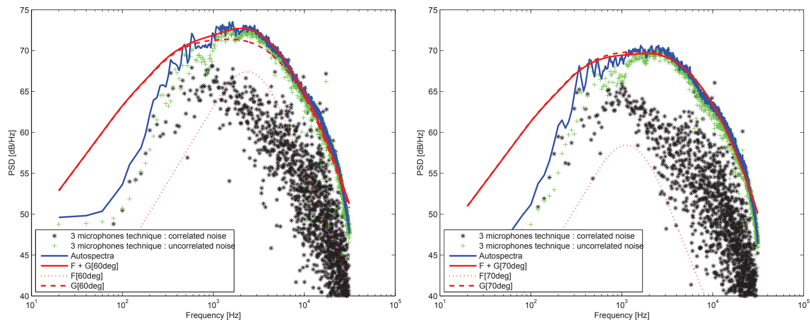

(a) (b)

Figure 27. (a) At 60° ; (b) At 70°.

At high angles, 90° and 120° in figure 28, we choose to represent the autospectra, the uncorrelated noise calculated with equation 18 and the Fine-Scale Similarity Spectra of Tam. There is a good match between Tam's FSS and the uncorrelated noise.

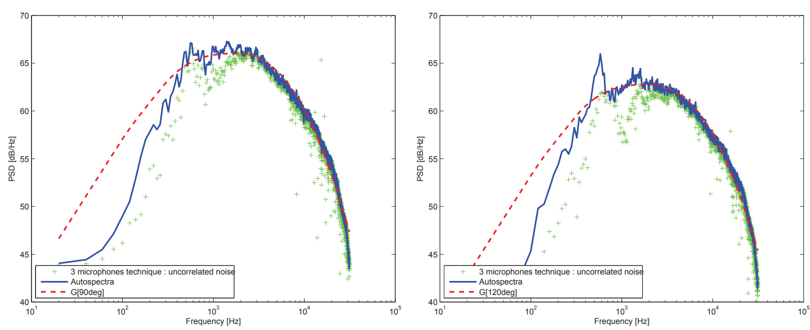

(a) (b)

Figure 28. (a) At 90° ; (b) At 120°.

A first conclusion could be that the three microphones technique is efficient to separate experimental jet noise database in two similarity spectra close to Tam's LSS and FSS. However, regarding equation 16, we notice that there are always three ways to calculate the correlated and uncorrelated noise of a microphone. For instance, take the microphone at 50°. To calculate G_{uu} and G_{nn}, one can choose the following three trio of microphones : 30°-40°-50° or 40°-50°-60° or 50°-60°-70°. Figure 29 shows the results. In one case the 'correlated' noise matches the LSS in another the 'uncorrelated' noise matches the LSS.

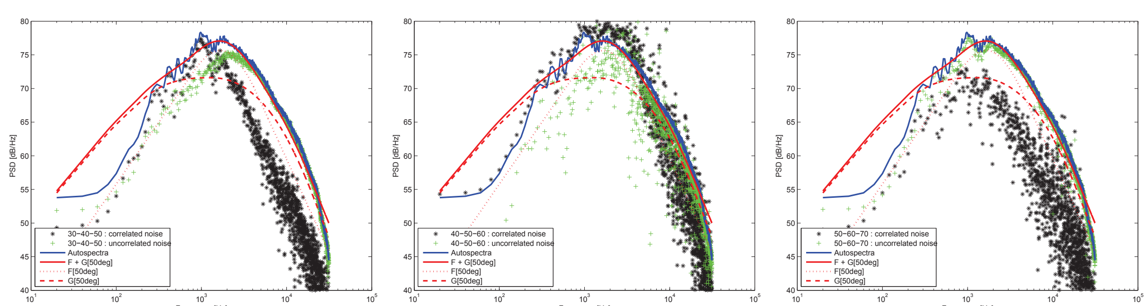

(a) (b) (c)

Figure 29. (a) Microphones at 30°-40°-50° ; (b) Microphones at 40°-50°-60° ; (c) Microphones at 50°-60°-70°.

Acknowledgments

The present work was initiated during the 3^{rd} IFFC held in Poitiers in 2008. It was supported by SNECMA and CNPq, National Council of Scientific and Technological Development - Brazil.

References

[1]Tam C., Viswanathan K., Ahuja K., Panda J. (2008) *The sources of jet noise: experimental evidence.* J. Fluid Mech., Vol.615, pp.253-292.

[2]Nance D., Ahuja K. (2009) *Experimentally separating jet noise contribution of large-scale turbulence from that of small-scall turbulence.* AIAA paper 2009-3213, 15^{th} AIAA/CEAS Aeroacoustics Conf., Miami, Florida.

[3]Papamoschou D. (2008) *Imaging of directional distributed noise sources.* AIAA proc. 2008-2885.

[4]Jordan P., Gervais Y. (2008) *Subsonic jet aeroacoustics : associating experiment, modelling and simulation* Exp. Fluids, Vol.44, pp.1-21.

[5]Goldstein M., Leib E. (2005) *The role of instability waves in predicting jet noise.* J. Fluid Mech., Vol.284, pp.37-72

[6]Crow S.C., Champagne F.H. (1971) *Orderly structure in jet turbulence.* J. Fluid Mech., Vol.48, pp.547-591.

[7]Moore C.J. (1977) *The role of shear-layer instability waves in jet exhaust noise.* J. Fluid Mech., Vol.80, pp.321-367.

[8]Michalke A., Fuchs H.V. (1975) *On turbulence and noise of an axisymmetric shear-layer.* J. Fluid Mech., Vol.70, pp.179-205.

[9]Mankbadi R., Liu J.T.C. (1984) *Sound generated aerodynamically revisited: large-scale structures in a turbulent jet as a source of sound.* Phil. Trans. R. Soc. Lond., Vol.311, pp.183-217.

[10]Crow S.C. (1972) *Acoustic gain of a turbulent jet.* Meeting Am. Phys. Soc., Div. Fluid. Dynamics, Univ. Colorado.

[11]Juvé D., Sunyach M., Comte-Bellot G. (1980) *Intermittency of the noise emission in subsonic cold jets.* J. Sound Vibration, Vol.71, pp.319-332.

[12]Guj G., Carley R., Camussi C. (2003) *Acoustic identification of coherent structures in a turbulent jet.* J. Sound Vibration, Vol.259, pp.1037-1065.

[13]Hileman J., Thurow B., Carabello E., Samimy M. (2005) *Large-scale structure evolution and sound emission in high-speed jets: real-time visualisation with simultaneous acoustic measurements.* J. Fluid Mech., Vol.544, pp.277-307.

[14]Cavalieri A., Jordan P., Gervais Y., Wei M., Freund J. (2010) *Intermittent sound generation in a free-shear flow.* AIAA paper 2010-3963, 16^{th} AIAA/CEAS Aeroacoustics Conf., Stockholm, Sweden.

[15]Grassucci D., Jordan P., Camussi R. (2010) *Combined wavelet and linear stochastic estimation analysis.* AIAA paper 2010-3954, 16^{th} AIAA/CEAS Aeroacoustics Conf., Stockholm, Sweden.

[16]Sandham N., Morfey C., Hu Z. (2006) *Sound radiation from exponentially growing and decaying waves.* J. Sound Vib., Vol.294, pp.355-361

[17]Cavalieri A., Jordan P., Agarwal A., Gervais Y. (2010) *Jittering wave-packet models for subsonic jet noise.* AIAA paper 2010-3957, 16^{th} AIAA/CEAS Aeroacoustics Conf., Stockholm, Sweden.

[18]Jordan P., Gervais Y. (2005) *Modelling self- and shear-noise mechanisms in inhomogeneous, anisotropic turbulence.* J. Sound Vib., Vol.279, pp.529-555.

[19]Farge M. (1992) *Wavelet transforms and their applications to turbulence.* Annual Rev. Fluid Mech., Vol.24, pp.395-458.

[20]Torrence C., Compo G. (1998) *A practical Guide to Wavelet Analysis.* Bulletin of the American Meteorological Soc., Vol.79, No.1.

[21]Shanno D.F., Phua K.H. (1980) *Minimization of Unconstrained Multivariate Functions.* ACM Transactions on Math. Software, Vol.6, No.4, pp.618-622.

[22]Crighton D.G., Huerre P. (1980) *Shear-layer pressure fluctuations and superdirective acoustic sources* J. Fluid Mech., Vol.220, pp.335-368.

[23]Chung J.Y. (1977) *Rejection of flow noise using a coherence function method.* J. Acoust. Soc. Am., Vol.62.